

Quantum support vector machines for classification and regression on a trapped-ion quantum computer

Teppei Suzuki^{1,*}, Takashi Hasebe¹, and Tsubasa Miyazaki¹

¹ *Technology Strategy Division, SCSK Corporation, Toyosu Front, 3-2-20 Toyosu, Koto-ku, Tokyo 135-8110, Japan*

(Dated: July 5, 2023)

E-mail: tep.suzuki@scsk.jp

Abstract: The quantum kernel method is one of the most important methods in quantum machine learning. In the present work, we investigate our quantum machine learning models based on quantum support vector classification (QSVC) and quantum support vector regression (QSVR), using a quantum-circuit simulator (with or without noise) as well as the IonQ Harmony quantum processor. A dataset containing fraudulent credit card transactions and image datasets (the MNIST and the Fashion-MNIST datasets) were used for the QSVC tasks, whereas a financial dataset and a materials dataset were used for the QSVR tasks. For the classification tasks, the performance of our QSVC models using the trapped-ion quantum computer with 4 qubits was comparable to that obtained from noiseless quantum-computing simulations, in agreement with the results of our device-noise simulations with various values for qubit-gate error rates. For the regression tasks, the use of a low-rank approximation to the noisy quantum kernel in combination with hyperparameter tuning in ϵ -SVR can be a useful approach for improving the performance and robustness of the QSVR models on the near-term quantum device. Our results suggest that the quantum kernel described by our shallow quantum circuit can be used for both QSVC and QSVR tasks, indicating its robustness to noise and its versatility to different datasets.

Keywords: quantum kernels, QSVM, QSVR, trapped-ion quantum computer

1. INTRODUCTION

The field of quantum technologies [1] has seen tremendous progress in recent years, with the potential to revolutionize a wide range of industries. One possible application of quantum computing is the field of quantum machine learning [2–4], which could potentially be used for classifying and recognizing complex patterns more efficiently than classical methods [5]. The quantum kernel method is a promising candidate in this field; in the method, quantum states described by quantum circuits are used to compute inner products between pairwise data points in the high-dimensional quantum feature space [6, 7]. The classification based on the quantum kernel method is known as quantum support vector machine (QSVM), which is a quantum analog of classical support vector machine (SVM) [8, 9] that has been used for a variety

of machine learning tasks. An advantage of QSVM with certain feature maps applied for classically hard problems has been mathematically analyzed for the regime of fault-tolerant quantum computing [10, 11]. On the other hand, current quantum computers are still noisy intermediate-scale quantum (NISQ) devices, which means that NISQ processors are error-prone and sometimes have to be mitigated by using several techniques [12, 13]. Nevertheless, with the aid of cloud computing technology, there has been growing interest in the quest for early practical applications of near-term devices [14].

Over the last few years, there has been remarkable progress in quantum hardware [15], opening the path for the implementation of NISQ algorithms. Previous studies on quantum kernels have explored the use of various quantum hardware platforms, such as superconducting qubits [6, 16–22], trapped-ion qubits [22], Gaussian Boson Sampling [23, 24], neutral-atom qubits [25], and nuclear-spin qubits [26]. Owing to quantum decoherence and the noise of quantum gates, one can typically perform a limited number of quantum operations on NISQ devices. In this regard, trapped-ion quantum processors seem to offer some advantages, thanks to long coherence time, all-to-all connectivity, and high-fidelity gate operations [14, 27]. Previous studies have demonstrated the implementation of different NISQ algorithms on trapped-ion quantum computers; in particular, researchers have recently used the IonQ Harmony quantum processor and reported results in quantum machine learning [28–30], finance [31], quantum chemistry [32, 33], and the generation of pseudo-random quantum state [34]. A recent study has shown the feasibility of implementing QSVM with a simple quantum circuit on a trapped-ion quantum computer [20]; nonetheless, further investigation is necessary for understanding the full potential of the quantum kernel method using a different quantum kernel and various datasets.

In the present work, we investigate the performance of quantum support vector classification (QSVC) and quantum support vector regression (QSVR) on a trapped-ion quantum computer, using datasets from different industry domains including finance and materials science, aiming to bridge the gap between potential quantum computing applications and real-world industrial needs. Here, we employ quantum kernels described by a shallow quantum circuit that can be implemented on the IonQ Harmony quantum processor and analyze the performance of the models, in comparison with that of the classical counterpart as well as with that obtained from noiseless quantum-circuit simulations.

The remainder of the paper is organized as follows. To estimate the number of quantum measurements necessary for the estimation of quantum kernels for reliable predictions, we first perform noiseless and noisy quantum-computing simulations before conducting quantum experiments. Next, we investigate the effect of noise on the performance of the QSVC models using noisy simulations with various values for qubit-gate error rates. Then we investigate QSVMs on the trapped-ion quantum processor. Herein, we train our QSVC models using a dataset containing fraudulent credit card transactions and image datasets (the MNIST dataset and the Fashion-MNIST [35] dataset). Also, we train our QSVR models using a financial market dataset and a dataset for superconducting materials. In the QSVR tasks, to reduce the effect of noise, we use a low-rank approximation of the noisy quantum kernel and carefully optimize hyperparameters in SVMs. We demonstrate that our quantum kernel can be used for both the QSVC and QSVR tasks for our datasets examined. Finally, we summarize our conclusions.

2. RESULTS

2.1 Quantum circuit and the quantum kernel method

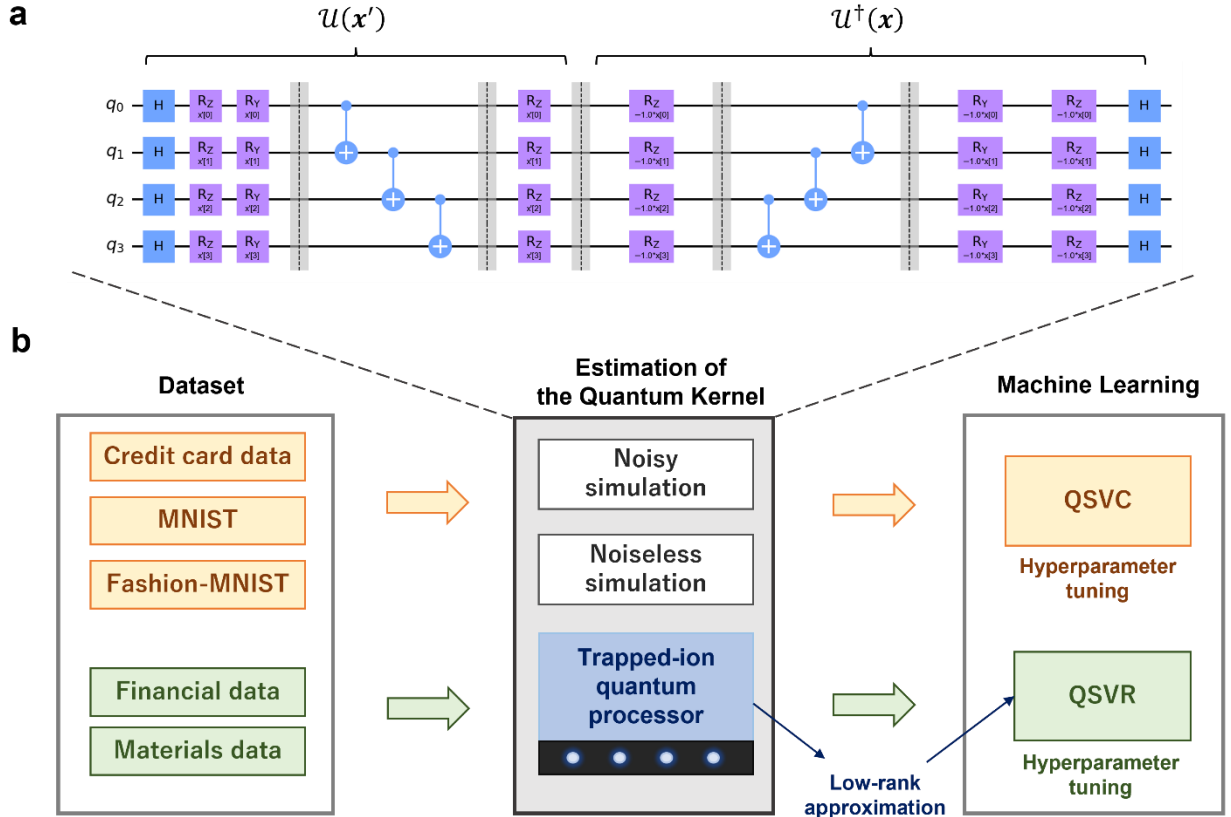


Figure 1: Schematic representation of our QSVC and QSVR workflows. (a) Shallow quantum circuit for estimating our quantum kernel $|\langle\phi(\mathbf{x})|\phi(\mathbf{x}')\rangle|^2$. Our quantum feature map $|\phi(\mathbf{x})\rangle = U(\mathbf{x})|0^{\otimes n}\rangle$ is given in Eq. (1) in the text. (b) Workflow for our QSVC and QSVR tasks (indicated by orange and green, respectively). For QSVC tasks, a credit-card dataset, the MNIST dataset, and the Fashion-MNIST dataset were used. For QSVR tasks, a financial dataset and a materials dataset were used. The estimation of the quantum kernel can be obtained using a quantum circuit simulator (either with or without noise) on a CPU (indicated by the white boxes) or computed using the IonQ Harmony (indicated by the blue box). Low-rank approximation was employed for QSVR tasks to reduce noise in the quantum kernel (for more details, see Sec. 2.3). The optimization of the hyperparameters in the models was also performed.

In the NISQ era, quantum gates are noisy, and two-qubit gates are typically an order of magnitude lower in fidelity compared to single-qubit gates. This means that one can only perform a limited number of quantum operations to ensure that the results are distinguishable from noise. In the present study, we use the following quantum feature map:

$$|\phi(\mathbf{x})\rangle = U(\mathbf{x})|0^{\otimes n}\rangle = \left(\bigotimes_{q=1}^n R_z(x_q)\right) U_{2^n}^{\text{ent}} \left(\bigotimes_{q=1}^n (R_y(x_q)R_z(x_q)H)\right) |0^{\otimes n}\rangle, \quad (1)$$

and

$$U_{2^n}^{\text{ent}} := \prod_{q=1}^{n-1} \mathbf{CNOT}_{q,q+1}. \quad (2)$$

Note that the connectivity of qubits in Eq. (1) is limited to their neighbors, resulting in $(n - 1)$ interactions. This can make quantum computation more amenable for near-term quantum devices. The quantum feature map given in Eq. (1) has been applied to image classification using a specialized quantum-kernel simulator, which is highly customized for this particular quantum circuit with the aid of field programmable gate arrays [36]. In quantum machine learning, the quantum kernel $K(\mathbf{x}, \mathbf{x}')$ described by the quantum feature map can be estimated by the inner product of the quantum states obtained from the two data points \mathbf{x} and \mathbf{x}' :

$$K(\mathbf{x}, \mathbf{x}') = |\langle \phi(\mathbf{x}) | \phi(\mathbf{x}') \rangle|^2 = |\langle 0^{\otimes n} | U^\dagger(\mathbf{x}) U(\mathbf{x}') | 0^{\otimes n} \rangle|^2. \quad (3)$$

The kernel represents the similarity between the two data points in the high-dimensional Hilbert space. Our quantum kernel entry can be estimated by using a shallow quantum circuit described in Fig. 1a. Once the quantum kernel is estimated by a quantum computer or a quantum-circuit simulator, we can use the kernel-based method (Fig. 1b). SVM is an important kernel-based method that is used for binary classification. The goal of SVC is to find the decision function. Suppose we are given a set of samples (\mathbf{x}_i, y_i) with $\mathbf{x}_i \in \mathbb{R}^d$ and $y_i \in \{\pm 1\}$, where d is the dimension of the input vector and the index i runs over $1, \dots, m$. To find the decision function, we solve the following problem [9]:

$$\max_{\alpha \in \mathbb{R}^m} W(\alpha) = -\frac{1}{2} \sum_{i,j=1}^m \alpha_i \alpha_j y_i y_j K(\mathbf{x}_i, \mathbf{x}_j) + \sum_{i=1}^m \alpha_i, \quad (4)$$

subject to

$$\alpha_i \in [0, C] \text{ and } \sum_{i=1}^m y_i \alpha_i = 0. \quad (5)$$

Here, the coefficients $\{\alpha_i\}$ are parameters determined through the optimization process. The patterns \mathbf{x}_i for which $\alpha_i > 0$ are called *support vectors* (SVs). The regularization parameter C controls the tradeoff between model complexity and its capacity to tolerate errors. The decision function $f(\mathbf{x})$ takes the form:

$$f(\mathbf{x}) = \text{sgn} \left(\sum_{i=1}^m y_i \alpha_i K(\mathbf{x}_i, \mathbf{x}) + b \right). \quad (6)$$

The bias b can be determined by the support vectors once the SVs and their Lagrange multipliers are obtained by the dual optimization [9].

2.2 Noiseless and noisy quantum simulations

To understand the effects of noise, we first employed a device-noise model provided by Qiskit Aer [37]. Here, the noise model is based on a depolarizing noise model, in which single-qubit gate errors and two-qubit gate errors are taken into account. Single-qubit errors consist of a single-qubit depolarizing error followed by a single-qubit thermal relaxation error, whereas two-qubit gate errors comprise a two-qubit depolarizing error followed by single-qubit thermal relaxation errors on both qubits in the gate. Hereafter, we denote them as p_1 and p_2 , respectively. In the context of the quantum kernel method, it is of particular importance to understand how noise affects the quality of the quantum kernel matrix and the prediction accuracy. To quantify this, we use the *alignment* between two kernels [38] defined by

$$A(K, K') = \frac{\langle K, K' \rangle_F}{\sqrt{\langle K, K \rangle_F \langle K', K' \rangle_F}}, \quad (7)$$

where $\langle P, Q \rangle_F$ is the Frobenius inner product between the matrices P and Q :

$$\langle P, Q \rangle_F = \sum_{ij} P_{ij} Q_{ij} = \text{Tr}\{P^T Q\}. \quad (8)$$

The alignment $A(K, K')$ can be viewed as the cosine of the angle between the two matrices viewed as vectors. By using the alignment of the noisy quantum kernel K^{noise} with the noiseless quantum kernel K , $A(K, K^{\text{noise}})$, we can conveniently measure the deviation of a noisy kernel from the noiseless one.

Using device-noise-model simulations, we investigated the robustness of our quantum kernel matrix in the presence of noise and the prediction performance (Fig. 2). In our noisy simulations, we varied the number of qubits from 4 to 12 in Eq. (1) and considered the following conditions for qubit-gate error rates: (i) $p_1 = 0.001$, $p_2 = 0.005$ and (ii) $p_1 = 0.01$, $p_2 = 0.05$. In Appendix A, we numerically show that 500 shots per kernel entry were enough to ensure the quality of our quantum kernel and to maintain reliable predictions; thus, 500 shots were conducted for each kernel entry throughout our simulations. To explore the applicability of our quantum kernel, three different datasets were considered: the credit card fraudulent transaction dataset, the NMIST dataset, and the Fashion-MNIST dataset. For the three datasets, the test accuracy obtained from the noisy quantum kernel was on par with that obtained from the noiseless quantum simulations, suggesting that the noise in the quantum kernel had minimal impact on the test accuracy of our QSVM models. This can be confirmed by the fact that the alignment was above 0.996, which may be partly due to the nature of our shallow quantum circuits. On the other hand, we are aware that our simulations based on the device noise model are only an approximation of real errors that occur on actual devices (In Section 2.3, we will demonstrate the performance of our QSVC models on the real quantum

device using 4 qubits).

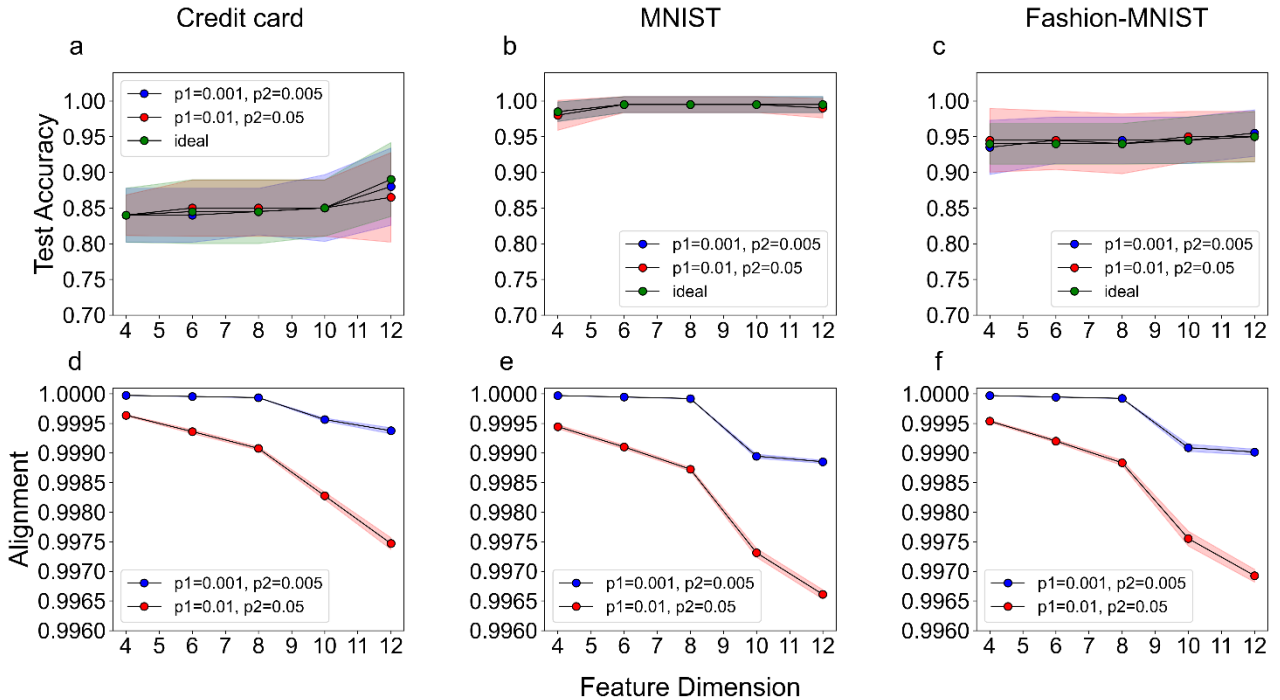


Figure 2: The dependence of the prediction performance of our QSVC models on the number of qubits from 4 to 12 (noisy simulations). Top panel: test accuracy for (a) credit card dataset, (b) MNIST dataset (binary classification of two labels: ‘0’ vs. ‘1’), and (c) Fashion-MNIST dataset (binary classification of two image categories: ‘T-shirt’ vs. ‘trouser’). Bottom panel: alignment of the noisy quantum kernel with the noiseless quantum kernel for (d) credit card dataset, (e) MNIST dataset, and (f) Fashion-MNIST dataset. In our device-noise-model simulations, we consider the following conditions for single- and two-qubit gate error rates: (i) $p_1 = 0.001, p_2 = 0.005$ (indicated by blue); (ii) $p_1 = 0.01, p_2 = 0.05$ (indicated by red). Five independent seeds for each dataset were used to obtain the statistical results. The number of training data was 40 and the number of test data was 20.

Next, we investigated how the device noise level affects the alignment and the test accuracy (Fig. 3). To this end, we performed device-noise-model simulations using 4 qubits for a range of qubit-gate error rates: $0.001 \leq p_1 \leq 0.55$ and $0.001 \leq p_2 \leq 0.55$. By comparing the alignment and the test accuracy, we found that, for certain regions ($p_1 < \approx 0.05$ and $p_2 < \approx 0.1$), our QSVC model can predict, even in the presence of noise (Fig. 3a and 3b). When qubit-gate error rates become relatively high, however, the noisy quantum kernel deviates from the ideal quantum kernel and thus the prediction performance begins to deteriorate rapidly. Given the fact that $p_1 \approx 0.001$ and $p_2 \approx 0.01$ for state-of-the-art NISQ devices, we can verify the prediction performance of our QSVC model on real quantum computers (which will be demonstrated in the next subsection). Our noise-model simulations suggest that the alignment between noiseless and noisy quantum kernels is an indicator of how reliably a QSVC model can predict using a NISQ device in comparison with its noiseless counterpart. In our QSVC model, if the alignment is higher than

0.98, then the QSVC model can make reliable predictions (Fig. 3c). To understand this more intuitively, one can recall that the alignment can be viewed as the cosine of the angle between the two matrices (viewed as vectors); in such a mathematical viewpoint, it means that the angle between noiseless and noisy kernels needs to be less than 11.5 degrees for reliable predictions on a noisy quantum device.

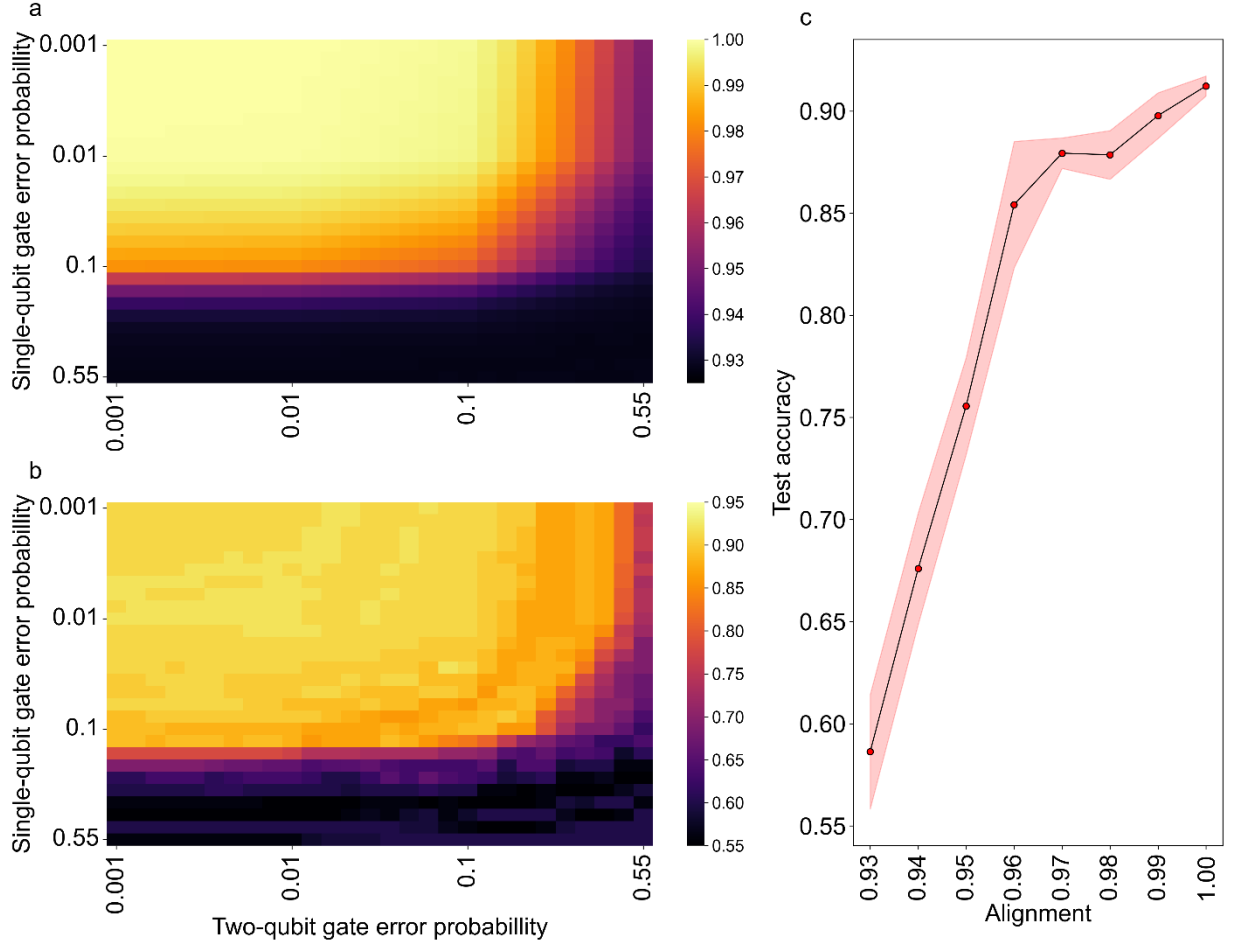


Figure 3: Effects of noise on (a) the alignment, (b) the test accuracy of the QSVC model, and (c) the correlation between the two. The device-noise-model simulations were performed using 4 qubits for a range of qubit-gate error rates: $0.005 \leq p_1 \leq 0.55$ and $0.005 \leq p_2 \leq 0.55$. The results suggest that our QSVC model is capable of making reliable predictions, if the alignment is higher than 0.98, which roughly corresponds to the condition that $p_1 < \approx 0.05$ and $p_2 < \approx 0.1$. The shaded area in part (c) indicates the standard deviation. The Fashion-MNIST dataset was used, and the number of training data was 40 and the number of test data was 20.

2.3 QSVC on the IonQ Harmony quantum computer

Having examined the results of the noise-model simulations, we now turn to our quantum experiments using the IonQ Harmony. The Gram matrices we obtained using the quantum device are shown in Fig. 4. To validate the quality of our noisy quantum kernels, we investigated the alignment of the noisy quantum kernel with the noiseless quantum kernel: the values for the alignment $A(K, K^{\text{noise}})$ were 0.986, 0.993, and 0.984 for the credit-card dataset, the MNIST dataset, and the Fashion-MNIST dataset, respectively. Since the three values were higher than 0.98, this suggests that the quantum kernel matrix entries were successfully estimated using the IonQ Harmony and indicates that reliable predictions can be made using our QSVC models on the quantum device (see also Fig. 3c).

Motivated by the reliable estimation of the quantum kernel on the IonQ Harmony, we trained QSVC models using the three datasets and validated the models using test data (Table 1). Our results show that the prediction performance of our QSVC models is maintained even in the presence of noise: test accuracies obtained using the quantum computer for the credit-card dataset, the MNIST dataset, and the Fashion-MNIST dataset were 70%, 100%, and 100%, respectively; this is the same performance of QSCV models with noiseless quantum kernels. This is consistent with the results of our noise-model simulations, in which predictions can be made using noisy quantum kernels with an alignment higher than 0.98. Furthermore, the performance of our QSVC models on the IonQ Harmony was comparable to that of classical SVR models. On a final note, we mention the number of support vectors (note that the decision boundary for the largest margin is determined solely by the position of the support vector): we found that there was a slight difference in the number of support vectors between QSVC models with noiseless kernels and those with noisy kernels on the IonQ Harmony, which might imply a subtle difference in the quantum feature map between noiseless simulations and actual quantum experiments, though both the QSVC models gave the same test accuracies.

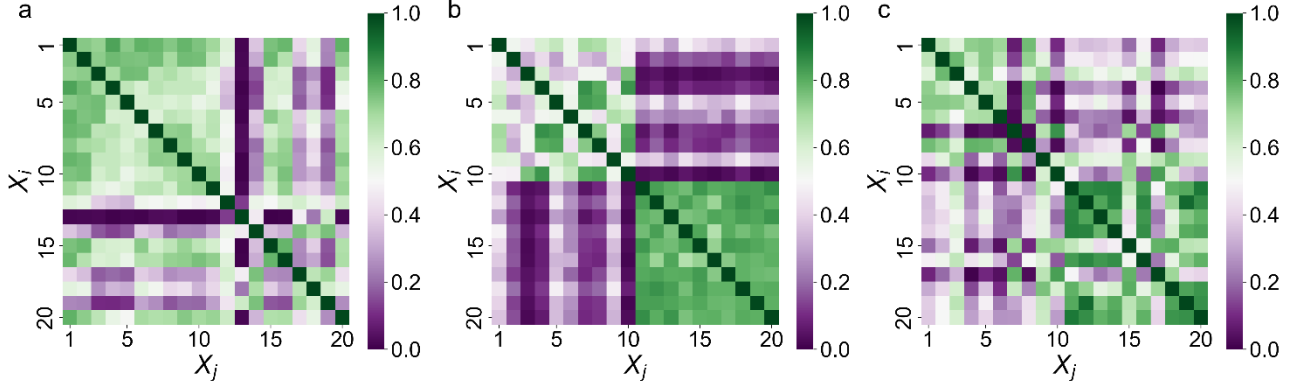


Figure 4: Quantum kernel matrices obtained using the IonQ Harmony quantum computer. (a) Credit-card dataset, (b) MNIST dataset, and (c) Fashion-MNIST dataset. For all the cases, the number of training data N was 20 and the number of measurements was 500. The values for the alignment of the noisy quantum kernel with the noiseless quantum kernel, $A(K, K')$, were 0.986, 0.993, and 0.984 for (a), (b), and (c), respectively. All of the values were higher than 0.98, which suggests that the quantum kernel matrix entries were successfully obtained using the IonQ quantum computer and indicates that reliable predictions can be made using our QSVC models on the quantum device (see also Fig. 3c).

Table 1 Model accuracy and the number of support vectors (SVs) for classical and quantum SVMs on three different datasets

Dataset	Model	Number of SVs	Acc. (train) (%)	Acc. (test) (%)
Credit card				
	Classical SVM	12	80	70
	QSVM (noiseless sim.)	11	85	70
	QSVM (IonQ Harmony)	12	100	70
MNIST				
	Classical SVM	16	100	100
	QSVM (noiseless sim.)	6	100	100
	QSVM (IonQ Harmony)	10	100	100
Fashion-MNIST				
	Classical SVM	8	100	100
	QSVM (noiseless sim.)	18	100	100
	QSVM (IonQ Harmony)	15	100	100

2.4 QSVC on the IonQ Harmony quantum computer

Datasets. Two different datasets were used in our QSVC tasks. One is a financial-market dataset (given in Appendix B). Financial data are characterized by high volatility and are often subject to noise caused by random fluctuations. In recent years, pandemics, geopolitical risks, and other microeconomic factors have

caused supply chain disruption, which led to price fluctuations of metal commodities such as nickel. In our QSVR model, the target variable y_i was the UK nickel price, and three attributes $\mathbf{x}_i \in \mathbb{R}^3$ were considered: the Shanghai Stock Exchange Composite (SSE) Index, West Texas Intermediate (WTI) crude oil, and US dollar index. Thus, in our QSVR model, 3 qubits were used for describing the quantum feature map on the Ion Q Harmony. Hereafter, the dataset is referred to as the *financial* dataset. The other is a superconducting-materials dataset [39]. Here, the target variable y_i was the critical temperature T_c for a broad class of superconducting materials. The original dataset contains 81 features (or descriptors); by using dimensionality reduction, four-dimensional vectors $\mathbf{x}_i \in \mathbb{R}^4$ were used as input data in this work (for more details of preprocessing, see section 4.1). Hence, 4 qubits were used for describing the quantum feature map. Hereafter, the dataset is referred to as the *materials* dataset.

Low-rank approximation. A popular approach to reducing the noise in the quantum kernel is to use a depolarizing model [1, 18, 22]; however, such a noise model may not necessarily be suited for real quantum devices, because there are various sources of noise. In addition, at the time of conducting our quantum experiment, we were not able to access the full control of native quantum gates of the trapped-ion quantum computer in the cloud service. In this work, we rather employed a postprocessing approach for error mitigation; in particular, we used low-rank approximation to reduce the noise in the quantum kernel. This can maintain the important information of the original matrix while reducing the noise. The low-rank approximation can be performed, for instance, by singular value decomposition (SVD). Recently, a study by Wang et al. [19] showed that the training performance of noisy quantum kernels is improved when spectral transformation (eigendecomposition) is adopted. Our idea is to reconstruct a quantum kernel \hat{K} from a noisy quantum kernel K by using eigendecomposition:

$$\hat{K} = \sum_{k=1}^r \mu_k \mathbf{u}_k \mathbf{u}_k^T, \quad (9)$$

where μ_k is the k th eigenvalue and \mathbf{u}_k is the corresponding k th eigenvector. The quantum kernel is approximated by summing over $\mu_k \mathbf{u}_k \mathbf{u}_k^T$, where the index k runs over $1, \dots, r$. Motivated by the important role of the alignment in QSVR (Fig. 2c), we argue that the optimal value for r can be determined by maximizing the alignment of the noisy quantum kernel with the noiseless one:

$$r^* = \underset{r \in \mathbb{N}}{\operatorname{argmax}} A(K, \hat{K}). \quad (10)$$

In the case of test data, we calculate a train-test kernel matrix, which is generally a rectangular matrix; hence, SVD was used for low-rank approximation.

We investigated the effects of low-rank approximation in improving the quality of the noisy quantum kernel (Fig. 5). For the financial dataset, the alignment had the maximum value of 0.993 at $r^* = 8$ (Fig. 5a). For the materials dataset, on the other hand, the alignment had the maximum value of 0.984 at $r^* =$

10 (Fig. 5d). The difference in the optimal r^* appears to be related to the difference in the nature of the datasets. For both cases, after the alignment peaked at the optimal r^* , the value for the alignment was gradually decreased and finally saturated for larger values of r . This can be confirmed by the fact that the contribution of eigenvectors for $k > r^*$ became substantially small (Fig. 5b and 5e), indicating that a large portion of the information is concentrated in eigenvectors up to r^* th. The results suggest that low-rank approximation can improve the quality of the noisy quantum kernel to some extent.

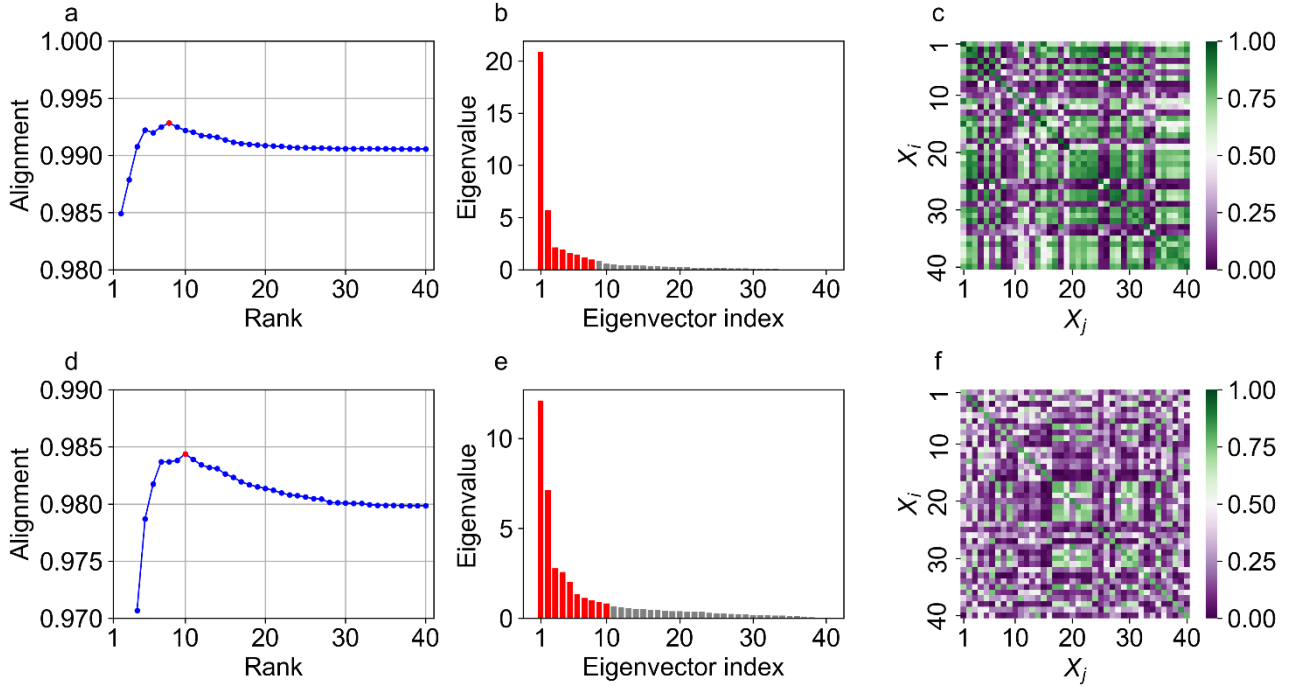


Figure 5: Use of spectral decomposition in improving the alignment of the quantum kernel obtained by the quantum device. Top (financial dataset): (a) alignment between the reconstructed quantum kernel and the noiseless quantum kernel with respect to the rank in the low-rank approximation (the alignment has the maximum value of 0.993 at $r^* = 8$, which is indicated by the red circle); (b) eigenvalues with respect to the eigenvector index (the first 8 components are indicated by the red bars); (c) reconstructed quantum kernel using the low-rank approximation ($r^* = 8$). Bottom (materials data): (d) alignment between the reconstructed quantum kernel and the noiseless quantum kernel with respect to the rank in the low-rank approximation (the alignment has the maximum value of 0.984 at $r^* = 10$, which is indicated by the red circle); (e) eigenvalues with respect to the eigenvector index (the first 10 components are indicated by the red bars); (f) reconstructed quantum kernel using the low-rank approximation ($r^* = 10$).

Optimization of hyperparameters in ε -SVR. The goal of ε -SVR is to find a regression function $f(\mathbf{x})$ that has at most ε deviation from the obtained targets $\{y_i\}$ for all the training data $\{\mathbf{x}_i\}$ [9]. Here, the hyperparameter ε defines a margin of tolerance (or ε -insensitive tube) where no penalty is associated with errors. In other words, any data points within this allowable error range are not considered errors, even if they do not fall directly on the regression line. This can be realized by using the ε -insensitive

loss function introduced by Vapnik [9], which is an analog of the soft margin in SVC. The linear ε -insensitive loss function can be described by

$$L_\varepsilon = \begin{cases} 0 & |y - f(\mathbf{x})| \leq \varepsilon \\ |y - f(\mathbf{x})| - \varepsilon & \text{otherwise} \end{cases}.$$

(11)

A smaller value of ε narrows the ‘no penalty’ region, making the model more sensitive to the training data, whereas a larger value of ε creates a wider tube, making the model less sensitive to the training data. An appropriate value of ε is related to the noise magnitude of data [40]. By using the Lagrangian formalism and introducing a dual set of variables, the primal problem in ε -SVR can be transformed into the dual optimization problem [9], which is described as follows:

$$\max_{\alpha, \alpha^* \in \mathbb{R}^m} W(\alpha, \alpha^*) = -\frac{1}{2} \sum_{i,j=1}^m (\alpha_i^* - \alpha_i)(\alpha_j^* - \alpha_j) K(\mathbf{x}_i, \mathbf{x}_j) - \varepsilon \sum_{i=1}^m (\alpha_i^* + \alpha_i) + \sum_{i=1}^m (\alpha_i^* - \alpha_i)y_i,$$

(12)

subject to

$$\alpha_i^*, \alpha_i \in [0, C] \text{ and } \sum_{i=1}^m (\alpha_i^* - \alpha_i) = 0.$$

(13)

Here, the coefficients $\{\alpha_i\}$ and $\{\alpha_i^*\}$ are parameters determined through the optimization process. The regularization parameter C determines the tradeoff between the complexity of the model and its capacity to tolerate errors. A larger value of C makes the model less tolerant of errors, which potentially leads to a risk of overfitting, whereas a smaller value of C helps the model more tolerant of errors, which tends to make the model less complex. By tuning the hyperparameters ε and C , one can find a good combination of parameters that makes the model more robust on new data, thus improving its generalization performance. The regression function takes the form [9]:

$$f(\mathbf{x}) = \sum_{i=1}^m (\alpha_i^* - \alpha_i) K(\mathbf{x}_i, \mathbf{x}) + b.$$

(14)

The bias b can be determined by the SVs, once the Lagrange multipliers are obtained by the dual optimization [9]. To access the performance of the model, we used the root mean square error (RMSE):

$$\text{RMSE} = \sqrt{\frac{1}{N} \sum_{i=1}^N (y_i - \hat{y}_i)^2}.$$

(15)

By performing a grid search for ε and C , we optimized the hyperparameters in ε -SVR using the quantum kernel that had been reconstructed by low-rank approximation (Fig. 6). For the financial dataset, the optimal values for the hyperparameters ε and C were 0.21 and 1.4, respectively, indicating that the ε -insensitive loss function was effective in enhancing the generalization of the model and reducing overfitting. The result is partly due to the nature of financial market data; that is, financial market data is characterized by high volatility owing to various factors such as geopolitical events and market sentiment and is often subject to noise caused by random fluctuations. For the materials dataset, on the other hand, the optimal values for the hyperparameters ε and C were 0.0 and 0.3, respectively. The optimal value of $\varepsilon = 0$ means that the allowable error range in the training data was unnecessary for this particular case. A possible reason may be that the impact of noise in the quantum kernel was effectively canceled through dimensionality reduction of input data and the use of low-rank approximation of the noisy quantum kernel. At the same time, a slightly smaller value of $C = 0.3$ made the model more robust against overfitting. For both cases, increasing the value for C (i.e., making the model fit the training data more tightly) did not improve the performance; instead, it had an adverse effect on the results (Fig. 6). Our results suggest that a combined approach that involves both the low-rank approximation to the noisy quantum kernel and the optimization of the hyperparameters in ε -SVR can be a useful strategy for improving the performance and robustness of the QSVR models.

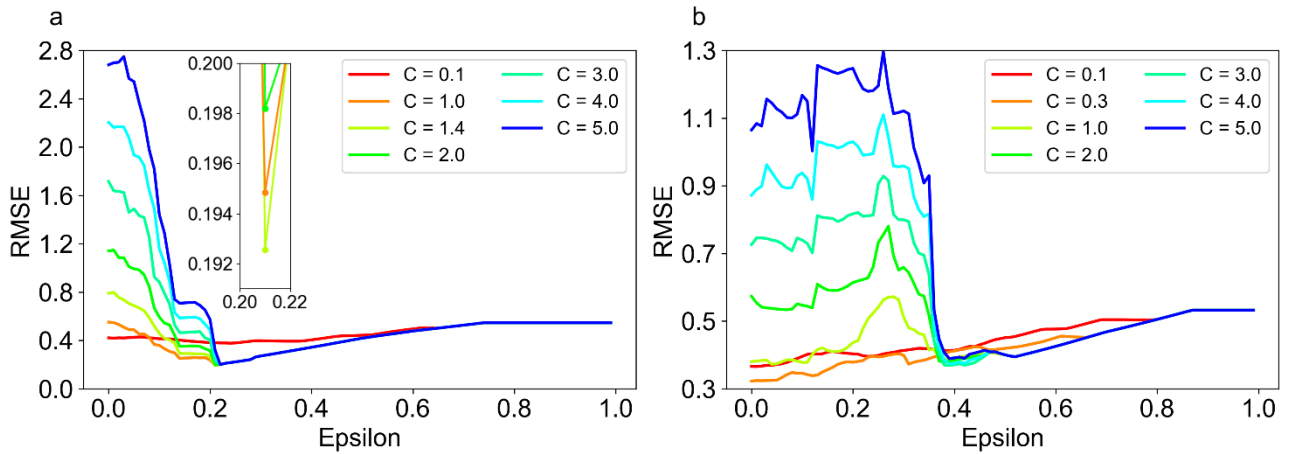


Figure 6: Optimization of the hyperparameters C and ε in ε -SVR using the quantum kernel reconstructed by low-rank approximation (see also Fig. 5). RSME with respect to ε for (a) financial dataset and (b) materials dataset. The optimal values for (ε, C) were $(0.21, 1.4)$ and $(0.0, 0.3)$ for (a) and (b), respectively.

Performance. Herein, we report the results of our QSVR models on the IonQ trapped-ion quantum computer and compare the performance with that obtained by the classical SVR tasks. For the financial dataset, the performance of our QSVR model using the noiseless simulation was comparable to that of our classical SVR model: the coefficient of determination R^2 for the classical SVR model was 0.930; whereas that for the QSVR model was 0.932. On the other hand, the coefficient of determination R^2 for the QSVR model using the IonQ Harmony was 0.868, which was 6.9% lower than that obtained by the noiseless

simulation. (We note that these machine learning models worked properly in predicting the financial price for a particular period in Appendix B, but the models may not guarantee the performance for another time window in the future.) For the materials dataset, the coefficient of determination for the classical SVR model was 0.728, whereas that for the QSVR using the noiseless simulation was 0.703. The coefficient of determination R^2 for the QSVR model using the real quantum device was 0.628, which was 10.7% lower than that obtained by the noiseless simulation. Since the alignment of the reconstructed quantum kernel for the materials dataset (0.984) was slightly lower than that for the financial dataset (0.993), the decrease in R^2 observed in the real device appeared to be more significant in the case of the former dataset. Overall, the presence of noise negatively affected the performance of QSVR tasks. Nonetheless, the results suggest that the alignment of the quantum kernel is a good indicator for accessing the performance of the quantum kernel method on the real quantum device.

Table 2 Coefficients of determination R^2 and RSME for classical and quantum SVR models on the financial dataset and the superconducting-materials dataset (for more details, see the text)

Dataset	Model	R^2	RSME
Financial data			
	Classical SVR	0.930	0.140
	QSVR (noiseless sim.)	0.932	0.138
	QSVR (IonQ Harmony)	0.868	0.192
Materials data			
	Classical SVR	0.728	0.276
	QSVR (noiseless sim.)	0.703	0.288
	QSVR (IonQ Harmony)	0.628	0.322

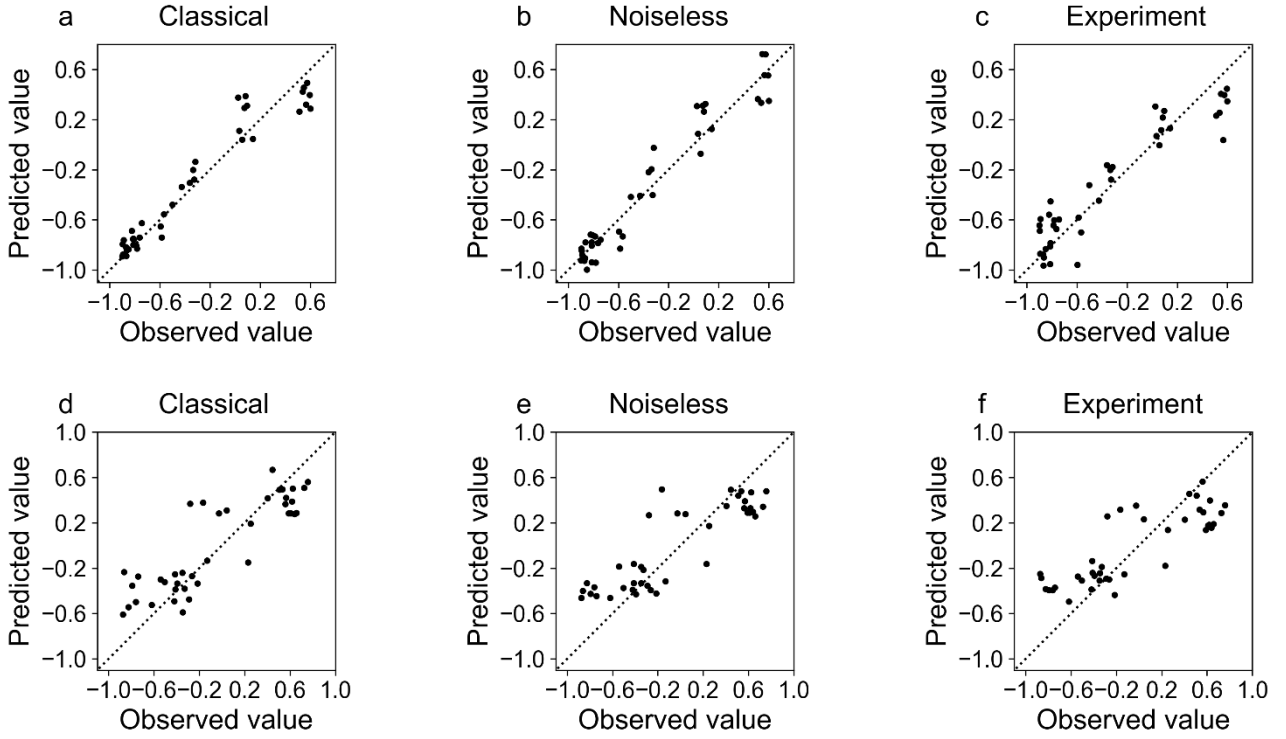


Figure 7: Parity plot between the predicted and observed values. Top panel (financial dataset): (a) classical SVR ($R^2 = 0.930$); (b) QSVR using the noiseless simulation ($R^2 = 0.932$); (c) QSVR using the IonQ Harmony ($R^2 = 0.868$). Bottom panel (materials dataset): (d) classical SVR ($R^2 = 0.728$); (e) QSVR using the noiseless simulation ($R^2 = 0.703$); (f) QSVR using the IonQ Harmony ($R^2 = 0.628$). For all cases, the number of test data was 40.

3. DISCUSSION

In the present work, we have investigated our QSVC and QSVR models, by performing quantum-circuit simulations (with and without noise) and using the IonQ Harmony quantum processor. For the classification tasks, we used the credit card dataset, the MNIST dataset, and the Fashion-MNIST dataset. The performance of our QSVC models obtained from the trapped-ion quantum computer using 4 qubits was comparable to that of the classical counterparts and that of the QSVC models obtained from the noiseless simulations. This suggests that the presence of noise in the quantum kernel did not significantly affect the test accuracy of the QSVM models. Our quantum experiments with 4 qubits were in good agreement with the results of our device-noise simulations, in which the prediction performance can be maintained from 4 to 12 qubits so long as the device noise level is lower than a certain threshold. Owing to the shallow quantum circuit and the limited number of qubits, however, our quantum feature map is not an example of quantum advantage. The robustness in the presence of noise can be interpreted by the fact that the alignment between the noiseless and the noisy quantum kernels was quite high. Hence, our noise-model simulations suggest that the alignment is a good indicator of how reliably a QSVM model on a NISQ device can make predictions in comparison with a noiseless counterpart.

In training our QSVR models, we used the financial dataset and the dataset for superconducting

materials. In particular, we investigated the role of the low-rank approximation and the effects of the hyperparameter tuning in ϵ -SVR, in improving the performance and robustness of the QSVM models. We found that the low-rank approximation was effective in reducing the effects of noise in the quantum kernel. The optimization of the hyperparameters in ϵ -SVR was also beneficial for mitigating the effect of noise. Therefore, a combined approach involving both the low-rank approximation to the noisy quantum kernel and the hyperparameter tuning in ϵ -SVR can be a useful approach for enhancing the performance and robustness of the QSVM models. We demonstrated that the quantum kernel described by our shallow circuit was versatile for both the QSVM and QSVR tasks for the different datasets we examined, which might have implications for designing quantum feature maps.

4. METHODS

4.1 Details of quantum-computing experiments

All the quantum calculations were carried out using the IonQ Harmony quantum processor provided by the Amazon Braket cloud service. To conduct our quantum-computing experiments, in the past few years, we have developed our quantum software development kit (SDK) called `PhiQonnect`, which is especially intended for quantum-kernel-based methods, including QSVC and QSVR. The quantum SDK utilizes open-source libraries such as IBM `Qiskit` (ver. 0.39.5) [37], `pytket` (ver. 1.11.1), which is a language-agnostic optimizing compiler provided by Quantinuum [41], `amazon-braket-sdk` (ver. 1.35.3) developed by Amazon Braket [42], and `scikit-learn` (ver. 1.2.1) [43], in which `LIBSVM` library [44] is included. All the quantum computations on the NISQ device were obtained using our SDK, which is available as open-source software (see CODE AVAILABILITY).

The computational details of our quantum experiments using the IonQ Harmony are summarized in Table 3. To obtain the quantum kernel estimation, the number of quantum measurements per kernel entry was set to 500 (we measured the quantum state in Z basis). This is supported by our noise-model simulations, in which 500 shots were shown to be enough to ensure the quality of the quantum kernel for the objective of this study (Fig. 2). To obtain the quantum kernel matrix for the training data, only the upper triangular entries were computed considering the symmetric nature of the quantum kernel, reducing a computational cost of using the quantum device. In training and testing our QSVC model, we used 20 data points for training and 10 data points (which are separate from the training data) for testing. A total of 105,000 ($= 20 \times \frac{21}{2} \times 500$) quantum measurements were conducted to obtain the quantum kernel and a total of 100,000 ($= 20 \times 10 \times 500$) shots were conducted to obtain the train-test kernel matrix. In training and testing our QSVR model, we used 40 data points for training and 40 out-of-sample data points for testing. A total of 410,000 ($= 40 \times \frac{41}{2} \times 500$) quantum measurements were conducted to obtain the quantum kernel and a total of 800,000 ($= 40 \times 40 \times 500$) shots were conducted to obtain the train-test kernel matrix.

To improve the performance of the machine learning models using the quantum kernels, we introduced a scaling hyperparameter λ in the quantum feature map (i.e., $\mathbf{x}^{(i)} \leftarrow \lambda \mathbf{x}^{(i)}$ in the quantum circuit). Such a hyperparameter can calibrate the angles of the rotation gates and affect the quantum feature map in the

Hilbert space. The hyperparameter can help improve the performance of the QSVM model [36, 45, 46]. In the present work, for the classification tasks, the hyperparameter λ was set to 1.0, whereas for the regression tasks, λ was set to 1.3.

Table 3 Details of quantum-computing experiments using the IonQ Harmony

Task	Dataset	λ	Number of data points		Number of total shots	
			train	test	train	test
Classification						
	Credit card	1.0	20	10	105,000	100,000
	MNIST	1.0	20	10	105,000	100,000
	Fashion-MNIST	1.0	20	10	105,000	100,000
Regression						
	Financial data	1.3	40	40	410,000	800,000
	Materials data	1.3	40	40	410,000	800,000

4.2 Preprocessing the materials dataset

We used a dataset for superconducting materials provided by Hamidieh [39], which was originally compiled by the National Institute of Materials Science in Japan. In this particular dataset, there are 81 features for the critical temperature T_c . To reduce the number of features that can be encoded into the NISQ device, the original 81-dimensional vector was reduced into the 4-dimensional vector using principal component analysis [47].

The distribution of critical temperature is concentrated in the low-temperature region. Such a non-normal distribution is not suited for building regression models. To overcome this, we used the Box–Cox transformation [48], which is a statistical technique used to transform a non-normal distribution into a normal distribution. It is often used in regression analysis to improve the performance of the model when the data does not follow a normal distribution [49]. The Box–Cox transformation is defined by the following equation:

$$y^{(\xi)} = \begin{cases} \frac{y^\xi - 1}{\xi} & (\xi \neq 0) \\ \log(y) & (\xi = 0) \end{cases} \quad (16)$$

Here, y is the original data, $y^{(\xi)}$ is the transformed data, and ξ is the Box–Cox transformation parameter. In this study, we used $\xi = 0.15084028$.

DATA AVAILABILITY

The datasets used in the present study are available at the following:

- a) Credit card fraud transaction: <https://www.kaggle.com/datasets/mlg-ulb/creditcardfraud>
- b) MNIST: <http://yann.lecun.com/exdb/mnist/index.html>
- c) Fashion-MNIST: <https://github.com/zalandoresearch/fashion-mnist>
- d) A financial-market dataset used for our QSVR task is tabulated in Appendix B.
- e) Superconductor materials: <https://archive.ics.uci.edu/ml/datasets/Superconductivity+Data>

CODE AVAILABILITY

A quantum software development kit for reproducing our quantum experiments is available at <https://github.com/scsk-quantum/phiqonnect>

REFERENCES

- [1] Nielsen, M. A. & Chuang, I. L. *Quantum Computing and Quantum Information, 10th Anniversary Ed.* (Cambridge University Press, Cambridge, UK, 2010).
- [2] Rebentrost, P., Mohseni, M. & Lloyd, S. Quantum support vector machine for big data classification. *Phys. Rev. Lett.* **113**, 130503 (2014).
- [3] Biamonte, J., Wittek, P., Pancotti, N., Rebentrost, P., Wiebe, N. & Lloyd, S. Quantum machine learning. *Nature* **549**, 195–202 (2017).
- [4] Cerezo, M., Verdon, G., Huang, H.-Y., Cincio, L. & Coles, P. J. Challenges and opportunities in quantum machine learning. *Nat. Comput. Sci.* **2**, 567–576 (2022).
- [5] Abbas, A., Sutter, D., Zoufal, C., Lucchi, A., Figalli, A. & Woerner, S. The power of quantum neural networks. *Nat. Comput. Sci.* **1**, 403–409 (2021).
- [6] Havlíček, V., Cárcamo, A. D., Temme, K., Harrow, A. W., Kandala, A., Chow, J. M. & Gambetta, J. M. Supervised learning with quantum-enhanced feature spaces. *Nature* **567**, 209–212 (2019).
- [7] Schuld, M. & Killoran, N. Quantum machine learning in feature Hilbert spaces. *Phys. Rev. Lett.* **122**, 040504 (2019).
- [8] Cortes, C. & Vapnik, V. Support-vector networks. *Mach. Learn.* **20**, 273–297 (1995).
- [9] Schölkopf, B. & Smola, A. J. *Learning with Kernels: Support Vector Machines, Regularization, Optimization, and Beyond.* (MIT Press, Cambridge, MA, 2002).
- [10] Liu, Y., Arunachalam, S. & Temme, K. A rigorous and robust quantum speed-up in supervised machine learning. *Nat. Phys.* **17**, 1013–1017 (2021).
- [11] Jäger, J. & Krems, R. V. Universal expressiveness of variational quantum classifiers and quantum kernels for support vector machines. *Nat. Commun.* **14**, 576 (2023).
- [12] Temme, K., Bravyi, S. & Gambetta, J. M. Error mitigation for short-depth quantum circuits. *Phys. Rev. Lett.* **119**, 180509 (2017).
- [13] LaRose, R., Mari, A., Kaiser, S., et al. Mitiq: A software package for error mitigation on noisy quantum computers. *Quantum* **6**, 774 (2022).
- [14] Bharti, K., Cervera-Lierta, A., Kyaw, T. H. et al. Noisy intermediate scale quantum algorithms. *Rev. Mod. Phys.* **94**, 015004 (2022).

[15] de Leon, N.-P., Itoh, K. M., Kim, D., Mehta, K. K., Northup, T. E., Paik, H., Palmer, B. S., Samarth, N., Sangtawesin, S. & Steuerman, D. W. Materials challenges and opportunities for quantum computing hardware. *Science* **372**, eabb2823 (2021).

[16] Peters, E., Caldeira, J., Ho, A., Leichenauer, S., Mohseni, M., Neven, H., Spentzouris, P., Strain, D. & Perdue, G. N. Machine learning of high dimensional data on a noisy quantum processor. *npj Quantum Inf.* **7**, 161 (2021).

[17] Heredge, J., Hill, C., Hollenberg, L. & Sevior, M. Quantum support vector machines for continuum suppression in B meson decays. *Comput. Softw. Big Sci.* **5**, 27 (2021).

[18] Hubregtsen, T., Wierichs, D., Gil-Fuster, E., Derk, P.-J. H., Faehrmann, P. K. & Meyer, J. J. Training quantum embedding kernels on near-term quantum computers. *Phys. Rev. A* **106**, 042431 (2022).

[19] Wang, X., Du, Y., Luo, Y. & Tao, D. Towards understanding the power of quantum kernels in the NISQ era. *Quantum* **5**, 531 (2021).

[20] Djehiche, B. & Löfdahl, B. Quantum Support Vector Regression for Disability Insurance. *Risks* **9**, 216 (2021).

[21] Krunic, Z., Flöther, F. F., Seegan, G., Earnest-Noble, N. D. & Shehab, O. Quantum kernels for real-world predictions based on electronic health records. *IEEE Trans. Quantum Eng.* **3**, 1–11 (2022).

[22] Moradi, S., Brandner, C., Coggins, M., Wille, R., Drexler, W. & Papp, L. Error mitigation for quantum kernel based machine learning methods on IonQ and IBM quantum computers. Preprint at <https://arxiv.org/abs/2206.01573> (2022).

[23] Schuld, M., Brádler, K., Israel, R., Su, D. & Gupt, B. Measuring the similarity of graphs with a Gaussian Boson Sampler. *Phys. Rev. A* **101**, 032314 (2020).

[24] Giordani, T., Mannucci, V., Spagnolo, N., Fumero, M., Rampini, A., Rodolà, E. & Sciarrino, F. Certification of Gaussian Boson Sampling via graphs feature vectors and kernels. *Quantum Sci. Technol.* **8**, 015005 (2023).

[25] Albrecht, B., Dalyac, C., Leclerc, L., Ortiz-Gutiérrez, L., Thabet, S., D'Arcangelo, M., Elfving, V. E., Lassablière, L., Silvério, H., Ximenez, B., Henry, L.-P., Adrien Signoles, A. & Henriet, L. Quantum feature maps for graph machine learning on a neutral atom quantum processor. *Phys. Rev. A* **107**, 042615 (2023).

[26] Kusumoto, T., Mitarai, K., Fujii, K., Kitagawa, M. & Negoro, M. Experimental quantum kernel trick with nuclear spins in a solid. *npj Quantum Inf.* **7**, 94 (2021).

[27] Bruzewicz, C. D., Chiaverini, J., McConnell, R. & Sagex, J. M. Trapped-ion quantum computing: progress and challenges. *Appl. Phys. Rev.* **6**, 021314 (2019).

[28] Johri, S., Debnath, S., Mocherla, A., Singk, A., Prakash, A., Kim, J. & Kerenidis, I. Nearest centroid classification on a trapped ion quantum computer. *npj Quantum Inf.* **7**, 122 (2021).

[29] Rudolph, M. S., Toussaint, N. B., Katabarwa, A., Johri, S., Peropadre, B. & Perdomo-Ortiz, A. Generation of High-Resolution Handwritten Digits with an Ion-Trap Quantum Computer. *Phys. Rev. X* **12**, 031010 (2022).

[30] Ishiyama, Y., Nagai, R., Mieda, S., Takei, Y., Minato, Y. & Natsume, Y. Noise-robust optimization of quantum machine learning models for polymer properties using a simulator and validated on the IonQ

quantum computer. *Sci. Rep.* **12**, 19003 (2022).

[31] Zhu, E. Y., Johri, S., Bacon, D., Esencan, M., Kim, J., Muir, M., Murgai, N., Nguyen, J., Pisenti, N., Schouela, A., Sosnova, K. & Wright, K. Generative quantum learning of joint probability distribution functions. *Phys. Rev. Res.* **4**, 043092 (2022).

[32] Nam, Y., Chen, J.-S., Pisenti, N. C., et al. Ground-state energy estimation of the water molecule on a trapped-ion quantum computer. *npj Quantum Inf.* **6**, 33 (2020).

[33] Zhao, L., Goings, J., Wright, K., Nguyen, J., Kim, J., Johri, S., Shin, K., Kyoung, W., Fuks, J. I., Rhee, J.-K. K. & Rhee, Y. M. Orbital-optimized pair-correlated electron simulations on trapped-ion quantum computers. *npj Quantum Inf.* **9**, 60 (2023).

[34] Cenedese, G., Bondani, M., Rosa, D. & Benenti, G. Generation of pseudo-random quantum states on actual quantum processors. *Entropy* **25**, 607 (2023).

[35] Xiao, H., Rasul, K. & Vollgraf, R. Fashion-MNIST: A novel image dataset for benchmarking machine learning algorithms. Preprint at <https://arxiv.org/abs/1708.07747> (2017).

[36] Suzuki, T., Miyazaki, T., Inaritai, T. & Otsuka, T. Quantum AI simulator using a hybrid CPU-FPGA approach. *Sci. Rep.* **13**, 7735 (2023).

[37] Aleksandrowicz, G., Alexander, T., Barkoutsos, P. et al. Qiskit: An open-source framework for quantum computing. <https://github.com/qiskit> (Accessed July 5, 2023).

[38] Cristianini, N., Shawe-Taylor, J., Elisseeff, A. & Kandola, J. On kernel-target alignment. In *Advances in Neural Information Processing Systems (NIPS)* 14. (2001).

[39] Hamidieh, K. A data-driven statistical model for predicting the critical temperature of a superconductor. *Comput. Mat. Sci.* **154**, 346–354 (2018).

[40] Zhang, K.-S. & Han, Z.-H. Support vector regression-based multidisciplinary design optimization in aircraft conceptual design. In *51st AIAA Aerospace Sciences Meeting including the New Horizons Forum and Aerospace Exposition*. (2023).

[41] Sivarajah, S., Dilkes, S., Cowtan, A., Simmons, W., Edgington, A. & Duncan, R. $t|ket\rangle$: A retargetable compiler for NISQ devices. *Quantum Sci. Technol.* **6**, 014003 (2020).

[42] Amazon Web Services. Amazon Braket SDK Python. <https://github.com/aws/amazon-braket-sdk-python> (Accessed July 5, 2023). (2022).

[43] scikit-learn library. <https://scikit-learn.org/stable> (Accessed July 5, 2023).

[44] Chang, C. C. & Lin, C. J. LIBSVM: a library for support vector machines. *ACM Trans. Intell. Syst. Technol.* **2**, 1–27 (2011).

[45] Shaydulin, R. & Wild, S. M. Importance of kernel bandwidth in quantum machine learning. *Phys. Rev. A* **106**, 042407 (2022).

[46] Canatar, A., Peters, E., Pehlevan, C., Wild, S. M. & Shaydulin, R. Bandwidth enables generalization in quantum kernel models. Preprint at <https://arxiv.org/abs/2206.06686> (2022).

[47] Subasi, A. & Gursoy, M. I. EEG signal classification using PCA, ICA, LDA and support vector machines. *Expert Syst. Appl.* **37**, 8659–8666 (2010).

[48] Sakia, R. M. The Box–Cox transformation technique: A review. *J. R. Stat. Soc. Series D Stat.* **41**, 169–178

(1992).

Appendix A: The number of quantum measurements per kernel entry

In Appendix A, we investigated how the number of measurements affects the kernel matrix and the prediction performance (Fig. A1). Three different datasets (the credit card fraudulent transaction dataset, the NMIST dataset, and the Fashion MNIST dataset) were examined. We considered the following conditions for qubit-gate error rates: (i) $p_1 = 0.001, p_2 = 0.005$ and (ii) $p_1 = 0.01, p_2 = 0.05$. In the case of the lower qubit-gate error rates, the alignment $A(K, K^{\text{noise}})$ remained high and almost unchanged. In the case of the higher qubit-gate error rates, the alignment was slightly improved by increasing the number of measurements. On the other hand, the test accuracy of QSVC models with the higher qubit-gate error rates was very similar to that in the case of the lower error rates. The results suggest that at least 500 shots per kernel entry are enough to ensure the prediction performance of our QSVC models. This is consistent with a recent work by Wang *et al.* [19], in which the accuracy is saturated at 500 shots per kernel entry. In the present work, the number of shots per kernel entry was set to 500 for our noisy numerical simulations as well as for quantum experiments using the real quantum device.

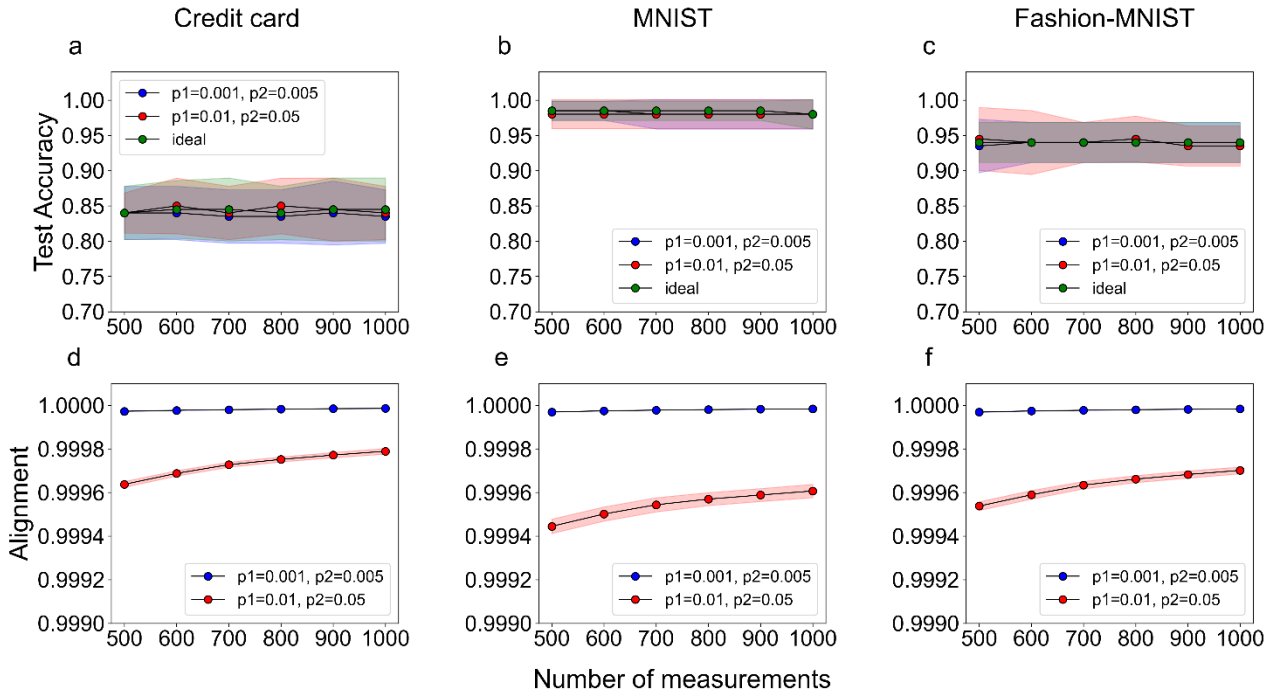


Figure A1: The effects of shots on the accuracy of QSVM. Top panel: test accuracy for (a) credit card dataset, (b) MNIST dataset, and (c) Fashion-MNIST dataset. Bottom panel: alignment of the noisy quantum kernel with the noiseless quantum kernel for (d) credit card dataset, (e) MNIST dataset, and (f) Fashion-MNIST dataset. In our device-noise-model simulations, we consider the following conditions for single- and two-qubit gate error rates: (i) $p_1 = 0.001, p_2 = 0.005$ (indicated by blue); (ii) $p_1 = 0.01, p_2 = 0.05$ (indicated by red). Five independent seeds for each dataset were used to obtain the statistical results. The number of training data was 80 and the number of test data was 40.

Appendix B: Financial dataset used for QSVR

Table B1 Financial dataset used for QSVR (training data)

Number	SSE Index	WTI Crude Oil	US Dollar Index	UK Nickel
1	3676.59	68.35	92.514	19506
2	3536.29	74.83	94.353	18342
3	3581.73	69.29	92.033	19789
4	3272.00	96.35	106.804	21613
5	3547.34	83.57	94.121	19448
6	3228.06	97.59	107.911	19802
7	3607.43	66.26	96.114	20030
8	3387.64	108.43	104.909	21824
9	3067.76	108.26	103.802	30114
10	3253.69	112.12	98.499	31583
11	3662.60	70.46	92.614	19623
12	3489.15	92.10	96.188	24396
13	3047.06	104.69	103.230	31771
14	3567.10	68.59	92.449	19332
15	3693.13	68.14	92.48	20190
16	3579.54	78.90	95.722	20734
17	3562.70	69.95	96.338	20141
18	3186.27	94.42	106.104	22492
19	3429.58	91.32	95.392	23398
20	3607.09	72.61	92.919	19401
21	3518.42	82.81	93.326	19574
22	3613.97	71.97	93.176	19358
23	3609.86	83.76	93.809	20306
24	3593.15	82.96	93.728	20050
25	3275.76	97.26	106.331	21700
26	3409.21	111.76	104.261	23158
27	3555.26	82.12	94.775	22176
28	3597.43	82.64	94.901	22064
29	3284.83	120.67	104.151	27264
30	3613.07	73.98	93.335	19387
31	3625.13	71.12	96.489	19615
32	3558.28	81.31	93.961	19294
33	3189.04	88.54	105.566	22210
34	3167.13	94.29	99.924	32483
35	3516.30	68.44	92.512	19656
36	3582.08	76.75	96.544	20336
37	3524.74	69.09	93.038	19678
38	3522.16	68.74	92.694	19011
39	3576.89	65.57	96.024	19946
40	3637.57	72.36	95.881	20230

Table B1 Financial dataset used for QSVR (test data)

Number	SSE Index	WTI Crude Oil	US Dollar Index	UK Nickel
1	3561.76	80.44	94.080	18918
2	3582.60	83.76	93.625	19739
3	3569.91	85.43	95.723	22073
4	3477.13	65.64	92.971	18893
5	2928.51	98.54	101.769	32636
6	3675.19	69.30	92.650	19713
7	3186.43	114.67	101.766	28392
8	3498.54	80.86	93.853	19162
9	3642.22	73.30	93.03	19351
10	3146.86	110.29	102.097	27732
11	3054.99	106.13	104.897	27810
12	3398.62	105.76	104.464	22698
13	3238.95	121.51	103.218	28023
14	3546.94	80.64	94.519	18978
15	3225.64	106.95	100.326	33175
16	3675.02	72.38	96.015	19624
17	3582.83	75.45	93.381	18946
18	3462.31	95.72	96.694	24282
19	3130.24	115.07	101.698	28284
20	3320.15	104.27	104.192	24038
21	3004.14	103.09	103.689	28185
22	3271.03	114.93	98.615	32380
23	3446.98	66.59	93.145	19193
24	3282.72	99.27	98.627	33223
25	3186.82	104.25	99.913	32981
26	3715.37	70.45	92.652	19726
27	3267.2	106.19	103.981	24449
28	3573.84	66.50	96.158	19953
29	3451.41	91.59	96.619	24361
30	3465.83	93.66	95.697	23406
31	3628.49	72.23	93.460	19221
32	3586.08	79.46	96.326	20383
33	3544.48	84.05	93.879	19702
34	3263.79	122.11	102.546	28855
35	3266.60	107.82	97.875	32893
36	3656.22	72.61	92.534	20016
37	3567.44	81.22	95.625	21794
38	3595.09	72.05	96.370	20189
39	3313.58	104.09	107.829	21880
40	3214.50	105.96	99.055	32725